Space-charge and current non-uniformities, and contact resistivity of end-bonded metal contacts to thin heavily doped semiconductor nanowires

Anvar A. Shukkoor, and Shreepad Karmalkar

Citation: Journal of Applied Physics **124**, 084502 (2018); doi: 10.1063/1.5041330
View online: https://doi.org/10.1063/1.5041330
View Table of Contents: http://aip.scitation.org/toc/jap/124/8
Published by the American Institute of Physics

Space-charge and current non-uniformities, and contact resistivity of end-bonded metal contacts to thin heavily doped semiconductor nanowires

Anvar A. Shukkoor[a] and Shreepad Karmalkar[b]
Department of Electrical Engineering, Indian Institute of Technology Madras, Chennai 600036, Tamil Nadu, India

(Received 24 May 2018; accepted 29 July 2018; published online 27 August 2018)

Prior work calculated the contact resistivity, ρ_{cN}, of *end-bonded* metal contacts on n-type silicon NanoWires (NWs) of radius, $R = 5$–10 nm and doping, $N_d = 10^{18}$–10^{20} cm^{-3}; it described the internal physics briefly and qualitatively, and considered long NWs and high barrier heights, $\phi_{b0} = 0.8$–1.0 V. The present work extends the ρ_{cN} calculations to low $\phi_{b0} = 0.4$–0.6 V contacts with long NWs, and to low to high $\phi_{b0} = 0.4$–0.8 V contacts with short NWs of length, $L_{NW} \leq$ long NW space-charge width. It calculates the space-charge and current distributions in contacts with $L_{NW} = 50$ nm–2 μm and low to high $\phi_{b0} = 0.4$–0.8 V to provide the following insights: (i) radial non-uniformity in space-charge width and current are high enough to violate the plane space-charge edge assumption employed to model NW junctions analytically. The non-uniformity peaks at N_d where the bulk depletion width $\approx 2.14R$ for large metals and small surface charge. (ii) Low ϕ_{b0} contacts are tunneling dominated, and their ρ_{cN} versus N_d behaviour differs qualitatively from that of high ϕ_{b0} contacts. (iii) Practical L_{NW} can be $\leq$long NW space-charge width, for $N_d \leq 10^{19}$ cm^{-3}. Shortening the L_{NW} reduces the space-charge non-uniformity and increases (reduces) the tunneling [generation-recombination (GR)] current. However, the current non-uniformity is unaffected, and the change in current or ρ_{cN} is disproportionately smaller than that in L_{NW}, since the tunneling or GR causing these occur over a small region near the junction which is less affected by NW shortening. All our calculations include the effects of contact geometry, surface defects, dielectric confinement, image force, and heavy doping. Our work provides an experimentalist clear qualitative understanding over a wide range of conditions. *Published by AIP Publishing.*
https://doi.org/10.1063/1.5041330

I. INTRODUCTION

NanoWire (NW) devices communicate with the outside world through metal contacts whose contact resistivity affects NW device characteristics.[1–3] This paper studies an *end-bonded*[4] metal contact, shown in Fig. 1, encountered in some NW devices and in the characterization of single or arrays of NWs.[5–10] The structure shown in Fig. 1(a) has a NW which is much longer than the space-charge width. Figure 1(b) shows a structure having a short NW whose length, L_{NW}, is comparable to or smaller than the space-charge width of the long NW structure in Fig. 1(a); on the side opposite to the metal contact, the NW is terminated by a wide n+ substrate (doping $= 5 \times 10^{20}$ cm^{-3}) on which the NW is realized. Analysis of the simple structure of Fig. 1(b) can give a feel for the charge distribution, current distribution, and contact resistivity in a NW contact which is a part of a device, e.g., contact to the ungated portion of a NW FET; in this case, other parts of the device limit the portion of the NW which can be influenced by the surrounding field from the contact. We denote the contact resistivity of the long NW structure in Fig. 1(a) as $\rho_{cN\infty}$ (∞ means long) and that of the short NW structure of Fig. 1(b) as ρ_{cN}.

Recently,[11] we presented numerical calculations of the doping dependence of $\rho_{cN\infty}$ of Al, Pt, and PtSi contacts[12–14] having a high intrinsic barrier height of $\phi_{b0} = 0.8$–1.0 V on *thin long* n-type silicon NWs of radius $R = 5$–10 nm (Refs. 7, 15, and 16) and *heavy* doping[4–6,8,15,17,18] of $N_d = 10^{18}$–10^{20} cm^{-3}, embedded in SiO_2; the following points were made:[11]

- $\rho_{cN\infty}$ should be estimated using the formula[8] $\rho_{cN\infty} = [dI/dV|_{V\to 0}]^{-1}\pi R^2$, where I is the total current through the junction area πR^2, rather than the more common formula[12] $\rho_{cN\infty} = [dJ/dV|_{V\to 0}]^{-1}$ based on a uniform current density, J, over the contact area; this is because, in such NW contacts, the space-charge edge and hence J are radially non-uniform.
- apart from tunneling which affects the contact resistivity, ρ_{cB}, of bulk contacts, space-charge generation-recombination (GR) current also affects $\rho_{cN\infty}$ at lower doping near 10^{18} cm^{-3}.

The above prior work[11] was focused on the calculation of $\rho_{cN\infty}$ which is a terminal characteristic. The work explained the calculated trends by barely touching upon the internal physical picture *qualitatively* in terms of the space-charge distribution, current distribution, and interplay of tunneling and GR currents. Moreover, the work did not consider commonly encountered contacts with either a short NW of length $L_{NW} <$ a few hundred nm,[19] or with NiSi, TiSi,

[a]Author to whom correspondence should be addressed: anvar9101987@gmail.com.
[b]Electronic mail: karmal@ee.iitm.ac.in.

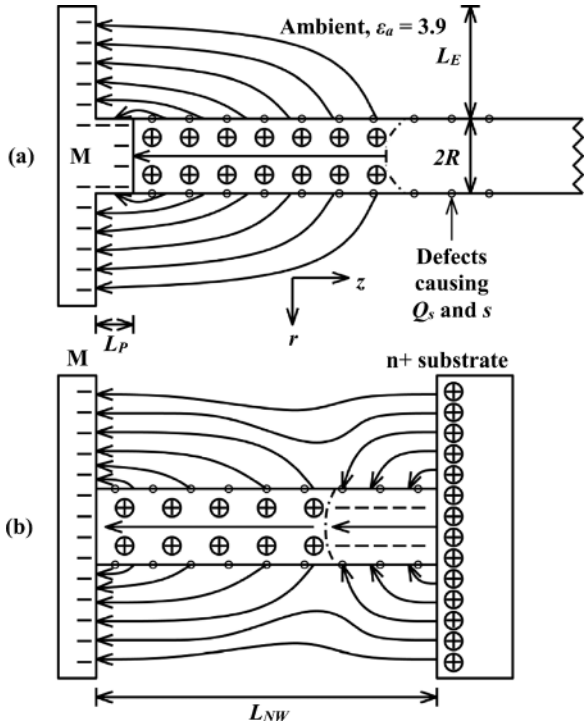

FIG. 1. Schematic of the metal contact to a long (a) and short (b) n-type semiconductor nanowire analysed in this paper, showing the geometrical parameters, charges, field lines, and surface defects, which are responsible for surface charge and recombination. The z-axis is the axis of the NW and its origin is located at the contact. In (b), doping of the n^+ substrate is $5 \times 10^{20}\,cm^{-3}$.

$ErSi_x$ or $YbSi_x$ metals[12,20,21] which have a low $\phi_{b0} = 0.4$–0.6 V to n-type silicon NWs.

The purpose of the present work is to provide a comprehensive physical insight into the operation of end-bonded contacts to long and short NWs by: (a) extending the ρ_{cN} calculations to low $\phi_{b0} = 0.4$–0.6 V contacts with long NWs, and to low to high $\phi_{b0} = 0.4$–0.8 V contacts with short NWs of length, $L_{NW} \leq$ long NW space-charge width; (b) calculating the internal physical picture of contacts over the wide range of $\phi_{b0} = 0.4$–0.8 V on n-type silicon NWs of $R = 5$–10 nm, $L_{NW} = 50$ nm–$2\,\mu$m and $N_d = 10^{18}$–$10^{20}\,cm^{-3}$ embedded in SiO_2. The internal physical picture consists of the space-charge and current non-uniformities, energy location of tunneling, spatial distribution of GR current, and relative contributions of tunneling and GR currents. The calculations are done using the TCAD (Technology Computer Aided Design) simulator. Our work provides an experimentalist clear qualitative understanding over a wide range of conditions.

Section II describes the device structure and the physics unique to the high surface to volume ratio of NWs. The simulation methodology is similar to that described in Sec. IV of our prior work;[11] its key features are summarized in the Appendix for the convenience of readers. Section III discusses the calibration of the simulator. Section IV discusses our results for contacts with long NWs regarding space-charge and current non-uniformities, role of tunneling and generation-recombination currents, and doping dependence of contact resistivity. Section V discusses similar results for the contacts with short NWs.

II. DEVICE STRUCTURE AND HIGH SURFACE TO VOLUME RATIO EFFECTS

Figure 1 gives the device structure. The geometrical parameters of the NW contact are its radial extension, L_E, and the cylindrical protrusion, L_P; L_E represents the effective metal electrode[22] over a NW of an array or a probe tip contacting a single NW; L_P represents[6] the metal penetration into the NW or a possible metallic nano-particle sandwiched between the NW and contact. The NW has a radius R, an n-type doping N_d, a permittivity ε_s, and when short, a length L_{NW}. The permittivity ε_a of the NW ambient governs the surrounding field which influences the charge and field conditions in the NW; in the present work, we have assumed a SiO_2 ambient whose $\varepsilon_a = 3.9$. The NW surface has a charge[23–25] Q_S and surface recombination velocity,[6] s, caused by surface defects. Thus, the parameters of a NW contact can be summarized as R, L_{NW}, L_E, L_P, Q_S, s, N_d, ε_s, and ε_a.

The high surface to volume ratio $= 2/R$ of the NW has the following consequences:

- The effective lifetime, τ_N, in the NW is reduced by orders of magnitude below the bulk lifetime, τ_B, due to magnification of the effect of surface recombination as per the formula[6] $\tau_N = (\tau_B^{-1} + 2s/R)^{-1}$; typically $s = 2.5 \times 10^5$ cm/s and $\tau_B = 1\ \mu$s yielding $\tau_N = 1$ ps for $R = 5$ nm.
- As compared to a bulk junction, the space-charge width is increased due to: (a) surrounding field lines[7,22,26,27] setup on the NW surface by the metal contact; (b) NW surface charge[23–25] Q_S of polarity opposite to that of the ionized dopants; and (c) reduced dopant ionization arising from increased ionization energy due to dielectric confinement[15,28,29] of dopants.

Figure 2 depicts possible mechanisms of current flow relevant to metal contacts on a heavily doped semiconductor NW. These include tunneling and generation-recombination, which cause currents I_T and I_{GR}, respectively. The much higher space-charge width in a NW junction (as compared to a bulk junction) cuts down I_T[7] but raises I_{GR}, which is further enhanced by $\tau_N \ll \tau_B$.[5,6,30] The sum $(I_T + I_{GR})$ remains much higher than thermionic emission, which can therefore be neglected; we have confirmed this in our simulations.

III. SIMULATOR CALIBRATION

We have simulated I_T and I_{GR} using TCAD SENTAURUS,[31] for an applied reverse bias of one thermal voltage, V_t, indicative of a small bias relevant for contact resistivity calculation. See the Appendix for the models, boundary conditions, and parameter values employed in the simulation.

To calibrate our I_T simulations, we used bulk contacts having the same doping and barrier height range as the NW contacts. This is because the contact resistivity ρ_{cB} of these contacts is known to be governed by tunnelling alone, and literature has a lot of measured and simulated data on ρ_{cB}. We calibrated our ρ_{cB} simulations for $\phi_{b0} = 0.4$–0.6 V in two ways. First, we confirmed that our simulations indeed reproduce the values of ρ_{cB} reported in Ref. 7 for GaAs contacts with $\phi_{b0} = 0.4$, 0.6 V at 300 K. Second, Fig. 3 shows that our

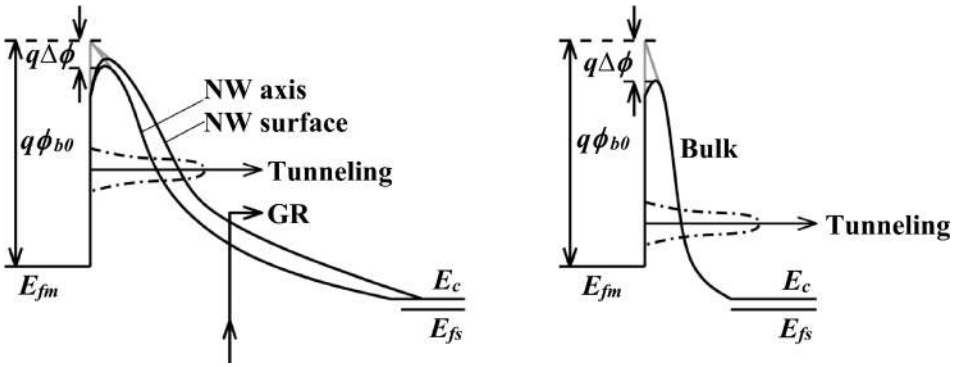

FIG. 2. Schematic of conduction band profiles, E_C, in a bulk contact and in a NW contact along its axis and surface at small reverse bias. Significant electron transport mechanisms, energy distribution of tunnelling electrons, and image force barrier lowering, $\Delta\phi$, are shown.

simulations match the measured ρ_{cB} of NiSi metal contacts on bulk n-silicon[32] over a wide doping range of $3\times10^{18} \le N_d \le 2\times10^{20}\,\mathrm{cm}^{-3}$ at $T=300\,\mathrm{K}$ using $\phi_{b0}=0.55\,\mathrm{V}$ and a doping independent tunneling effective mass $m=0.3m_0$.[14,33] Our ϕ_{b0} value is close to the value of 0.53 V used in Ref. 34 to match their simulation to the same measured data. Figure 3 also gives our calibration of ρ_{cB} simulations for Al contacts with $\phi_{b0}=0.8\,\mathrm{V}$ reported in our previous work.[11]

Calibration of our I_{GR} simulations was confirmed by the reasonably close match between our simulations of the effective generation width in the space-charge region of a bulk junction for a reverse bias of V_t with that reported in Ref. 35. This width corresponds to the part of the space-charge region where the electron and hole concentrations are less than the intrinsic concentration. See the I_{GR} calibration of our previous work[11] for more details.

IV. RESULTS AND DISCUSSION FOR A LONG NANOWIRE

We simulated n-type silicon NW contacts with $R=5$, 10 nm, $\phi_{b0}=0.4$, 0.8 V, and $N_d=10^{18}$–$10^{20}\,\mathrm{cm}^{-3}$ under a small reverse bias $=V_t$ relevant for contact resistivity calculation, at $T=300\,\mathrm{K}$. Unless stated otherwise, other parameters employed in our simulation are: $L_E=350\,\mathrm{nm}$, $L_P=0$, $\varepsilon_d/\varepsilon_0=3.9$, $Q_s=0$, $m=0.3m_0$, $\tau_B=1\,\mu\mathrm{s}$, and $s=2.5\times10^5\,\mathrm{cm/s}$ which yield $\tau_N=1$, 2 ps for $R=5$, 10 nm. Models and boundary conditions employed in simulations are given in the Appendix.

A. Space-charge non-uniformities

The unique features of the space-charge distribution in heavily doped NW contacts can be discerned from Fig. 4, which shows a schematic of this distribution along the NW length for long and short NWs for $N_d>10^{18}\,\mathrm{cm}^{-3}$. Define the space-charge width as the distance from the junction where space-charge falls to 50% of its maximum occurring at the junction. Focusing on the curves for the long NW, we find that the space-charge width at the surface, $W_{S\infty}$, is higher than that at the axis, $W_{A\infty}$. To investigate this phenomenon further, Fig. 5(a) shows the calculated distributions for $R=5\,\mathrm{nm}$ and different $N_d\ge10^{18}\,\mathrm{cm}^{-3}$. Previous theoretical nanowire junction analyses, e.g., Refs. 5–7, have been restricted to $N_d\le10^{18}\,\mathrm{cm}^{-3}$, and have centered on the enhancement and *axial* non-uniformity of the space-charge, assuming it to be *radially* uniform, i.e., $W_{S\infty}\approx W_{A\infty}$. In Fig. 5(a), these conditions are seen to apply at $N_d=1\times10^{18}\,\mathrm{cm}^{-3}$. However, at higher N_d, the space-charge width as well as the tail beyond are much higher at the surface than at the axis. Figure 5(b) gives the radial contours of the space-charge width at the doping levels considered in Fig. 5(a).

The physical origin of the above radial non-uniformity in space-charge width can be traced to the coexistence of radial and axial fields. This can be seen with the help of Gauss's law with cylindrical symmetry and fully depleted space-charge inside the NW, given by

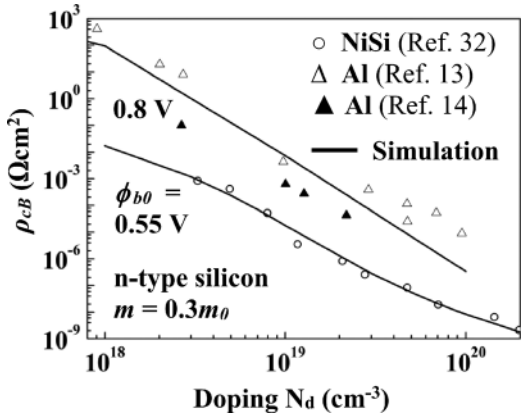

FIG. 3. Calibration of our TCAD simulations (lines) using measured resistivity (points) reported in literature for Al[13,14] and NiSi[32] contacts on bulk n-type silicon at $T=300\,\mathrm{K}$.

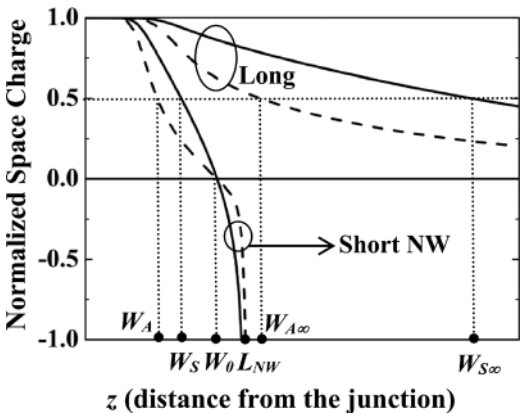

FIG. 4. Schematic of the normalized space-charge distribution along the NW axis (dashed line) and surface (solid line), defining the various space-charge widths in contacts with long and short NWs.

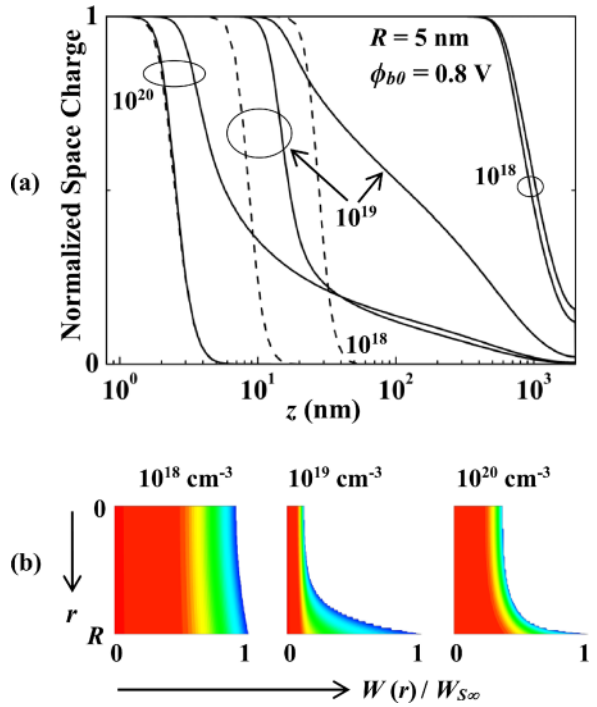

FIG. 5. (a) Simulated normalized space-charge distribution as a function of distance from the contact to a long NW (solid line) and a bulk contact (dashed line) at different doping levels. The solid line with lower space-charge width corresponds to the axis and the other to the surface. (b) Radial variation of the space-charge width $W(r)$ normalized to its surface value $W_{S\infty}$, for doping levels of (a). The colour variation from red to blue amounts to space-charge variation from its maximum to 50% of the maximum value. See the first para of Sec. IV for values of parameters other than those shown here.

$$\frac{E_r}{r}+\frac{\partial E_r}{\partial r}+\frac{\partial E_z}{\partial z}=\frac{qN_d}{\varepsilon_s}, \tag{1}$$

where E_r and E_z are radial and axial fields. If the space-charge is induced predominantly by the radial field E_r, then the $\partial E_z/\partial z$ term would be negligible and the charge picture would be similar to a fully depleted side-bonded contact with radially uniform space-charge. Similarly, a radially uniform space-charge analogous to that of a planar junction would exist, if the space-charge is predominantly due to the axial field E_z, wherein the radial terms of (1) are negligible. Since the potential drop from the metal contact to any point on the space-charge edge is the same = built-in voltage for all r, a radially non-uniform space-charge width must mean that the solution of Eq. (1) has radially varying E_z. This is possible only if both the radial and axial terms of Eq. (1) are significant, i.e., the space-charge is due to both E_r and E_z. Further, E_r must have a non-linear radial variation, so that first two terms of the LHS and thus E_z would be a function of r.

An important implication of the above large radial variation of the space-charge width is that it is not possible to define a unique space-charge width for junctions between a heavily doped NW and metal. Recall[5,22,26,36,37] that a plane space-charge edge was a key assumption in the derivation of an analytical model for the space-charge width in moderately doped NW junction arrays. The curved nature of the space-charge edge [Fig. 5(b)] in heavily doped NW junctions would necessitate the identification of an alternate assumption to derive an analytical model for the space-charge region in these junctions. To aid the derivation of such an analytical model and for use in NW device design until such a derivation becomes possible, Figs. 6(a) and 6(b) reports the calculations of $W_{S\infty}$ and $W_{A\infty}$ as a function of N_d for different R and ϕ_{b0}. Figure 6(c) shows that the ratio $W_{S\infty}/W_{A\infty}$, which represents the degree of radial space-charge non-uniformity, is a peaked function of N_d. Also, the ratio decreases with reduction in L_E due to the reduction in the surrounding field, and the peak is almost non-existent for $L_E = 25$ nm.

We can derive a closed-form estimate of the N_d corresponding to the peak ratio for large L_E and small Q_S in Fig. 6(c), by analyzing the distributions of the radial field at the surface, E_R, and the axial field at the axis, E_A, over the NW space-charge region at the peak points. By way of example, Fig. 6(d) shows the E_R and E_A at the peak point for $R = 5$ nm and $\phi_{b0} = 0.8$ V. Let E_{Am} denote the maximum value of E_A occurring at the junction and f the fraction of the NW space-charge contributing to E_A so that the fraction $(1–f)$ contributes to E_R. Based on Gauss's law, we can write

$$E_{Am}=\frac{qN_dW_{A\infty}}{\varepsilon_s}\cdot f, \quad E_R=\frac{qN_dR}{2\varepsilon_s}\cdot(1-f). \tag{2}$$

Figure 6(d) shows that we can approximate E_A to be linear as a function of distance and E_R to be constant over $W_{A\infty}$. From Eq. (2), constancy of E_R implies constancy of f with distance. Noting that the area under the E_A distribution is equal to (built-in potential plus reverse bias of V_t) $\approx \phi_{b0}$, and the space-charge width in a bulk contact with the same doping and barrier height as the NW contact can be written as $W_B = \sqrt{2\varepsilon_s\phi_{b0}/(qN_d)}$, we get

$$W_{A\infty}=W_B/\sqrt{f}. \tag{3}$$

Considering that the non-uniformity is created by the coexistence of radial and axial fields, it is of interest to examine the ratio $k = E_R/E_{Am}$. From Eq. (2) and Eq. (3), we can write k as

$$k=\frac{R}{W_B}\left(\frac{1-f}{2\sqrt{f}}\right), \tag{4}$$

which can be transformed as

$$\frac{W_B}{R}=\frac{1-f}{2k\sqrt{f}}. \tag{5}$$

For the four cases shown in Fig. 6(c), at the N_d corresponding to the peak points, we calculated f using the numerically simulated value of $W_{A\infty}$ from Figs. 6(a) and 6(b) in Eq. (3), and then k from Eq. (4). We found that f lies in the range 0.26–0.52 and k in the range 0.18–0.31, but the ratio W_B/R in Eq. (5) lies within 15% of 2.14. Hence, at the peak point, we approximate Eq. (5) as the following simple relation for W_B in terms of R, or equivalently, N_d in terms of R and ϕ_{b0}

$$W_B\approx 2.14R \Rightarrow N_d\approx 0.44\frac{\varepsilon_s\phi_{b0}}{qR^2}. \tag{6}$$

Table I gives the values of the peak ratio and the doping at which this peak is attained, from Fig. 6(c) as well as from

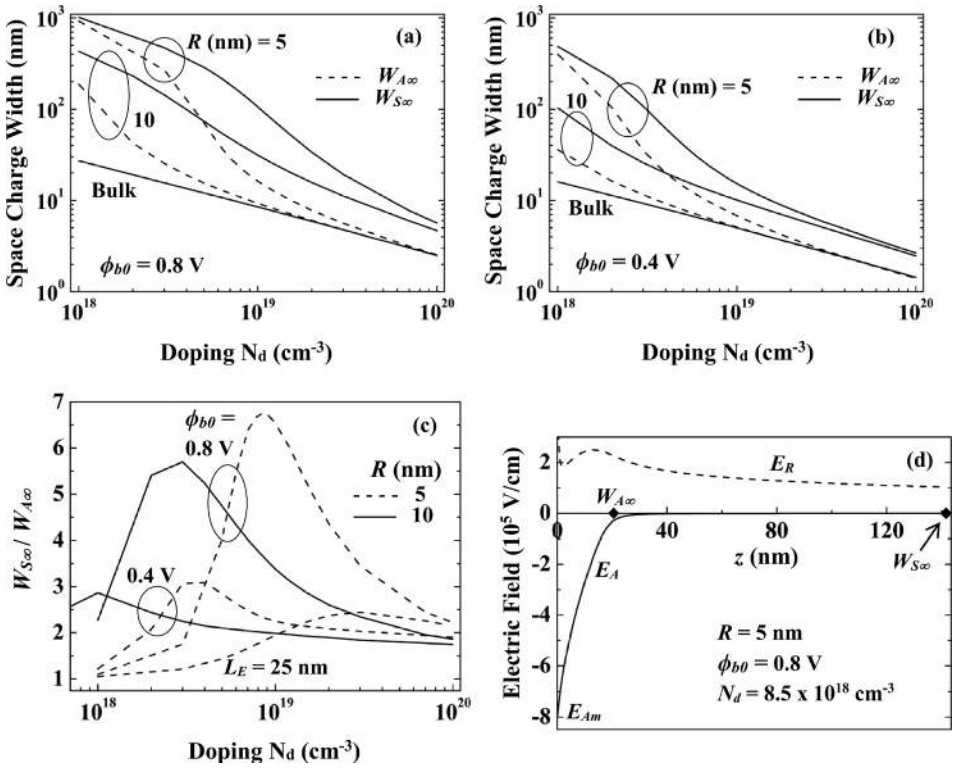

FIG. 6. (a) and (b) Doping dependence of the simulated space-charge width in contacts to long NWs. The bulk space-charge width is shown for comparison. (c) Doping dependence of radial non-uniformity of the simulated space-charge width, represented by the ratio of the space-charge width at the surface, $W_{S\infty}$, to that at the axis, $W_{A\infty}$. (d) Distribution of the radial field at the surface, E_R, and the axial field at the axis, E_A, over the NW space-charge width, $W_{S\infty}$. See the first para of Sec. IV for values of parameters other than those shown here.

Eq. (6). For $W_B \gg 2.14R$ or low N_d, the surrounding field penetrates deep into the NW, while at the other extreme of $W_B \ll 2.14R$ or high N_d, the surrounding field penetrates too little, leading to low non-uniformity in either case.

B. Generation-recombination and tunneling currents

The simulator estimates I_T using the non-local electron tunneling model, as per which the tunneling rate between the junction and a point, in a direction perpendicular to the junction area, is represented as a net generation rate G_T in the electron continuity equation.[38] On the other hand, the I_{GR} is estimated based on the SRH (Shockley-Reed-Hall) theory, where the electron and hole time constants τ_n and τ_p are both set equal to τ_N to capture the effect of high surface recombination. In order to identify the dominant current mechanism (see Fig. 2) in the metal-NW junction, Fig. 7 shows the conduction band profile, E_C, generation rate equivalent of tunneling, G_T, and SRH generation rate G_{SRH} along the NW axis for a reverse bias of V_t and different N_d and ϕ_{b0}. We have considered a NW with $R = 5$ nm by way of example.

In Figs. 7(a) and 7(b), the peak of E_C lies below the top of the barrier ϕ_{b0} due to image force barrier lowering, $\Delta\phi$, which increases with the peak electric field or gradient of E_C at the junction, and hence with N_d. The value of E_C corresponding to the peak G_T represents the energy location of peak emission depicted by the horizontal arrow representing tunneling in Fig. 2; analogously, the energy width of this emission is derived by projecting the effective generation width from the z-axis on to E_C. Using this approach, we can see that, independent of the value of ϕ_{b0}, the energy location of peak emission or tunneling is close to the top of the barrier for $N_d = 1 \times 10^{18}\,\mathrm{cm}^{-3}$ and near the middle of the barrier for $N_d = 1 \times 10^{19}\,\mathrm{cm}^{-3}$ indicating thermionic field emission in these cases; the peak emission is near the bottom of the barrier or the Fermi-level for $N_d = 1 \times 10^{20}\,\mathrm{cm}^{-3}$ indicating field emission. Figure 7(c) shows the G_{SRH} for $N_d = 1 \times 10^{18}\,\mathrm{cm}^{-3}$ alone, for which it turns out to be significant as will be explained shortly. The G_{SRH} peak location lies within 75 nm from the junction. In Figs. 7(a)–7(d), for both G_T and G_{SRH}, we define the effective generation width as the distance between the locations on the z-axis where the generation rate falls to 10% of its peak. Based on the peak location and effective width, we find that the SRH generation happens close to the junction within <12% of the space-charge width $W_{S\infty} \approx W_{A\infty}$ shown in Fig. 6(a). The area under the generation rate represents current density, which when integrated over the NW cross-section yields the current. This is how the tunneling current, I_T, is derived from G_T, and generation-recombination current, I_{GR}, is derived from G_{SRH}.

Consider the situation for $\phi_{b0} = 0.8$ V. For $N_d = 10^{18}\,\mathrm{cm}^{-3}$, the peak G_{SRH} [see Fig. 7(c)] is more than 100 times higher and its effective width ~20 times higher than those of G_T [see Fig. 7(a)], indicating the dominance of I_{GR} over I_T. However, similar simulations for $N_d = 10^{19}\,\mathrm{cm}^{-3}$ and $10^{20}\,\mathrm{cm}^{-3}$ show that I_T dominates over I_{GR} by more than two orders of magnitude at these doping levels. For

TABLE I. Parameters related to the peak space-charge non-uniformity point in Fig. 6(c).

			Doping (10^{18} cm^{-3}) at peak	
R (nm)	ϕ_{b0} (V)	Peak ratio from Fig. 6(c)	From Fig. 6(c)	From Eq. (6)
5	0.4	3.1	3.5	4.4
	0.8	6.7	8.5	8.8
10	0.4	2.9	1.0	1.1
	0.8	5.7	3.0	2.2

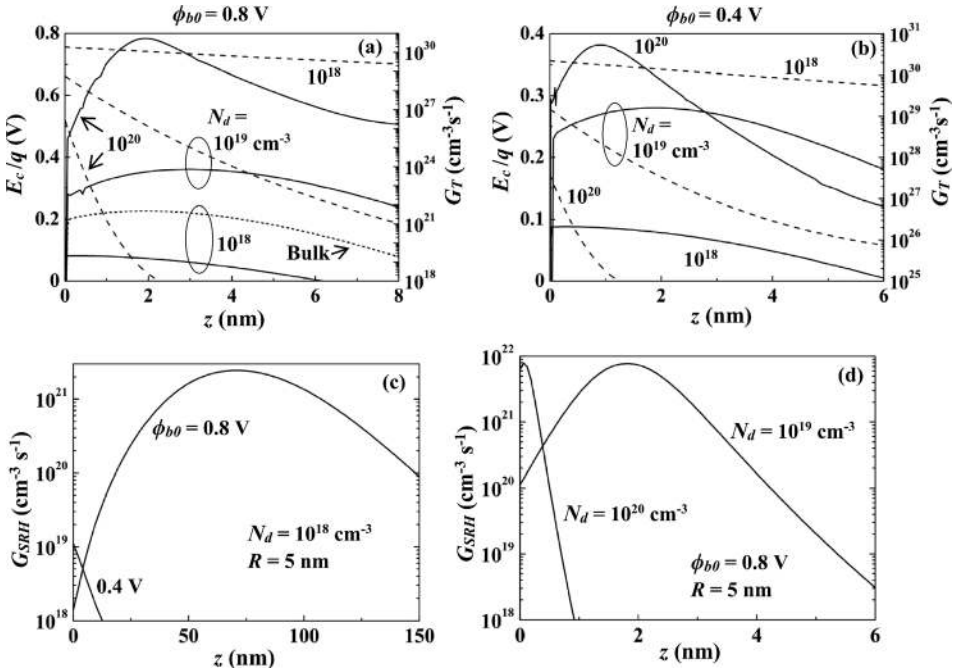

FIG. 7. Axial variation of the simulated conduction band edge, E_C (dashed line) and generation rate, G_T, representing tunnelling (solid line) in contacts to long NWs with $R = 5$ nm, for different doping levels and barrier heights $\phi_{b0} = 0.8$ V (a) and 0.4 V (b). $E_C = 0$ represents the metal Fermi-level. Axial variation of the simulated SRH generation rate, G_{SRH}, at different doping levels is given in (c) and (d). See the first para of Sec. IV for values of parameters other than those shown here.

$\phi_{b0} = 0.4$ V, I_T dominates over I_{GR} by more than six orders of magnitude at all doping levels in the range $N_d = 10^{18}$–10^{20} cm^{-3}. In Fig. 7(c), G_{SRH} is much smaller at $\phi_{b0} = 0.4$ V than at $\phi_{b0} = 0.8$ V, because 0.4 V < half of silicon bandgap = 0.55 V; consequently, throughout the NW space-charge region, the hole concentration, p, is much less than the electron concentration, n, implying the absence of a point where $p = n$ around which SRH generation occurs.

C. Current non-uniformities

The axial and radial current distributions in the NW can be explained in the light of radial non-uniformity in the space-charge region and behaviors of I_{GR} and I_T discussed so far. Some prior studies[5–7] on NWs have approximated the current density to be uniform over the area of the cross-section. As we show below, this approximation breaks down for N_d and R considered in this work.

Figure 8 gives the axial distribution of the current density, $|J_z|$, directed along the NW length, at the axis and the surface; this corresponds to a situation where I_{GR} is dominant, and is chosen for illustration since its features include those observed when I_T dominates. The location where the $|J_z|$ distribution at the axis crosses that at the surface coincides with the G_{SRH} peak location in Fig. 7(c). From this location, the generated holes move towards the junction while the generated electrons move away due to the axial field [see Fig. 1(a)]; simultaneously, the radial electric field moves the holes towards the surface and electrons towards the axis. Thus, close to the junction, the $|J_z|$ is due to holes and higher at the surface than at the axis, while away from the junction, $|J_z|$ is due to electrons and higher at the axis than at the surface. Much farther away from the junction, the $|J_z|$ at the axis and surface approach each other due to progressive fall in the radial field. In a nutshell, $|J_z|$ due to electrons tends to be uniform far away from the junction, but radially non-uniform with higher value at the axis than the surface as the junction is approached. This feature associated with the electron current is applicable even when I_T dominates, since tunneling current in an n-type NW is due to electrons alone, and so is common to all values of N_d and ϕ_{b0}. However, as we discuss below, when I_T dominates, the radial non-uniformity in G_T accentuates the radial non-uniformity of $|J_z|$ due to the radial electric field.

Figure 9(a) shows the detailed radial variation of $|J_z|$ in a normalized form for $R = 5$ nm, $\phi_{b0} = 0.4$, 0.8 V, $N_d = 10^{18}$, 10^{20} cm^{-3} and an in-between N_d value at which the space-charge non-uniformity is the maximum (see Table I). At $N_d = 1 \times 10^{18}$ cm^{-3}, the non-uniformity is the smallest regardless of whether $\phi_{b0} = 0.4$ V for which I_T dominates or $\phi_{b0} = 0.8$ V for which I_{GR} dominates. This is because, as argued above, this non-uniformity is radial field related; simulations confirm that at $N_d = 1 \times 10^{18}$ cm^{-3}, G_{SRH} and G_T are approximately constant radially because $W_{S\infty}$ and $W_{A\infty}$ are almost the same [see Fig. 6(c)]. For higher N_d, where I_T

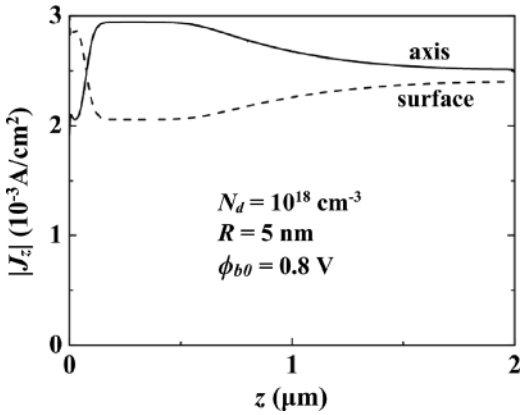

FIG. 8. Variation of the simulated axial current density along the NW axis and surface as a function of distance from the contact to a long NW, where generation-recombination dominates over tunnelling. See the first para of Sec. IV for values of parameters other than those shown here.

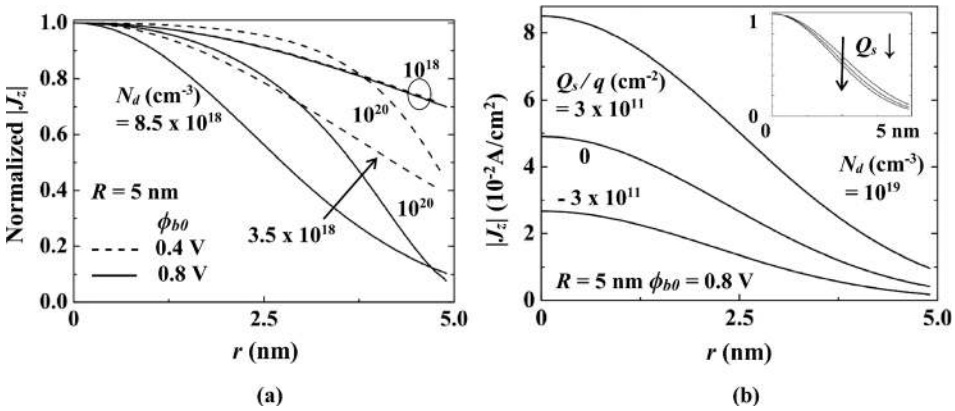

FIG. 9. (a) Radial non-uniformity of the normalized axial current density at different doping levels and barrier heights in a contact to a long NW. (b) Axial current density at different surface charges. Normalized variation is given in the inset. See the first para of Sec. IV for values of parameters other than those shown here.

dominates regardless of ϕ_{b0}, the non-uniformity in $|J_z|$ is higher and peaks at N_d corresponding to peak space-charge non-uniformity. This $|J_z|$ non-uniformity is therefore linked to non-uniformity in space-charge width, and hence in G_T, apart from the radial field. Simulations show that peak G_T decreases from axis to surface by 7.2–23 times for $N_d = 10^{19}$–$10^{20}\,\mathrm{cm}^{-3}$. This is because G_T depends strongly on the E_C distribution. Smaller electric field along the NW surface causes lesser image force barrier lowering $\Delta\phi$ (see Fig. 2) and higher tunneling distance, both of which reduce the tunneling probability. It is seen that, when non-uniformity peaks, for $R = 5\,\mathrm{nm}$, the current density at the axis is 2.5 (10) times that at the surface for $\phi_{b0} = 0.4$ (0.8) V; for $R = 10\,\mathrm{nm}$, the current density at the axis is 2.6 (13) times higher than at the surface.

Figure 9(b) illustrates the effect of Q_S on the radial distribution of $|J_z|$ when I_T dominates. It is seen that positive (negative) Q_S which increases (decreases) the effective n-type doping, raises (lowers) the current due to reduction (expansion) in space-charge width. However, the current distribution plotted in a normalized form as in the inset of Fig. 9(b) shows that Q_S does not affect radial non-uniformity.

D. Contact resistivity

In a previous work,[11] we discussed the doping dependence of $\rho_{cN\infty}$ of Al, Pt, and PtSi contacts[12–14] which have a high $\phi_{b0} = 0.8$–1.0 V to n-type Si. In the present work, we focus on the $\rho_{cN\infty}$ of NiSi, TiSi, $ErSi_x$, and $YbSi_x$ contacts[12,20,21] which have a low intrinsic barrier height of $\phi_{b0} = 0.4$–0.6 V to n-type NW, and point out how these contacts behave differently than those with higher barrier heights studied in our previous work.[11]

Figure 10(a) shows the doping dependence of ρ_{cB} and $\rho_{cN\infty}$ for $R = 5\,\mathrm{nm}$ and large L_E. For $\phi_{b0} = 0.4$–0.6 V, it is seen that both $\rho_{cN\infty}$ and ρ_{cB} decrease monotonically over the entire doping range. This is because I_T dominates over I_{GR} in bulk junctions, as well as in NW junctions with these ϕ_{b0} as discussed above; I_T is known to increase with doping. Further, $\rho_{cN\infty}$ is higher than ρ_{cB} since NW junctions have a

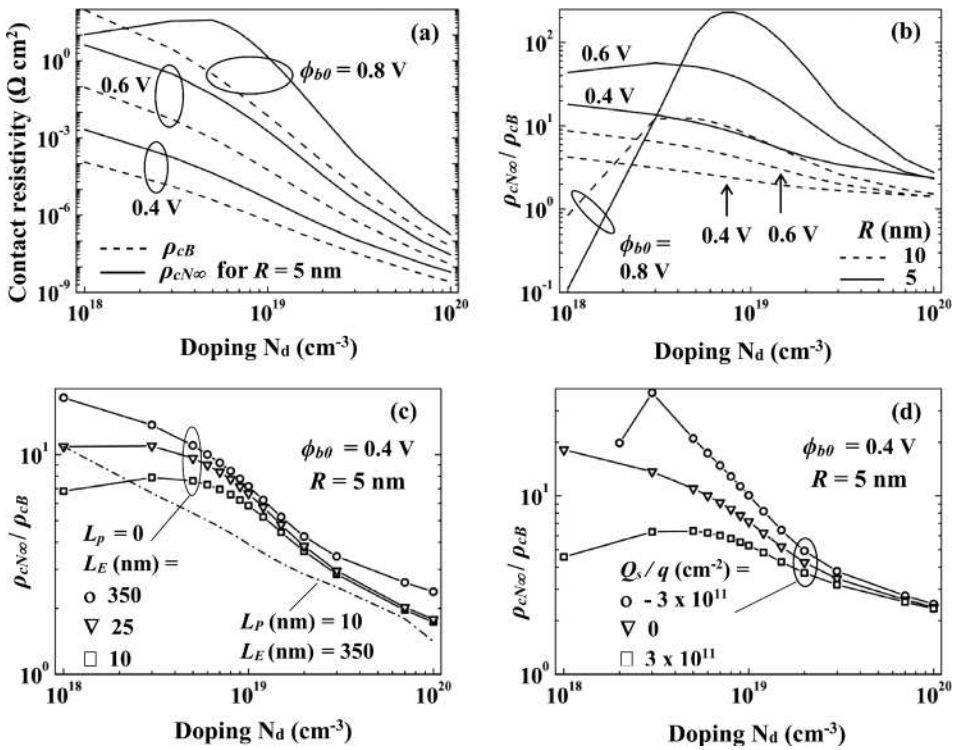

FIG. 10. (a) Simulated doping dependence of the resistivity $\rho_{cN\infty}$ of contacts to long NWs and ρ_{cB} of bulk contacts at different barrier heights and $T = 300\,\mathrm{K}$. (b) Doping dependence of the simulated ratio $\rho_{cN\infty}/\rho_{cB}$ at different barrier heights and NW radii. (c) Same as (b) for different values of contact extension, L_E, and metal protrusion, L_P. (d) Same as (b) for different values of surface charge, Q_S. See Ref. 11 for results similar to (c) and (d) at $\phi_{b0} = 0.8\,\mathrm{V}$. See the first para of Sec. IV for values of parameters other than those shown here.

higher space-charge width and hence a lower I_T than bulk junctions.[7,11] In contrast, for $\phi_{b0} = 0.8$ V, $\rho_{cN\infty}$ is seen to be less than ρ_{cB} for $N_d < 2 \times 10^{18}$ cm^{-3} and increasing with doping up to $N_d = 5 \times 10^{18}$ cm^{-3}. Our previous work[11] attributed this to the dominance of I_{GR} in the NW junction in this doping range. The present work illustrates this feature with the help of the G_{SRH} distribution in the NW [see Fig. 7(c)] and G_T distributions in the bulk and NW [see Fig. 7(a)]. The area under the G_{SRH} distribution is seen to be much higher than that under bulk G_T, which in turn is much higher than that under NW G_T. The area under G_{SRH} is high because the NW has a much higher space-charge width and lower lifetime than a bulk junction. Figures 7(c)–7(d) shows that the area under the G_{SRH} distribution, and hence I_{GR}, decreases with doping. This is why $\rho_{cN\infty}$ increases with doping up to $N_d = 5 \times 10^{18}$ cm^{-3}. The fall in $\rho_{cN\infty}$ beyond this doping is due to the dominance of I_T which increases with doping.

It is of interest to discuss doping dependence of the ratio $\rho_{cN\infty}/\rho_{cB}$ given in Figs. 10(b)–10(d). A model of this ratio allows one to predict $\rho_{cN\infty}$ from measured or modeled ρ_{cB}.[13,39] Moreover, this ratio depends on device physics alone, since the process and measurement related variations in $\rho_{cN\infty}$ and ρ_{cB} cancel each other out in this ratio, when $\rho_{cN\infty}$ and ρ_{cB} correspond to similar processes or extraction procedures. In Fig. 10(b), $\rho_{cN\infty}/\rho_{cB}$ decreases with N_d monotonically for $R = 5$ nm, $\phi_{b0} = 0.4$ V, and $R = 10$ nm, $\phi_{b0} \leq 0.6$ V, where the current is dominated by I_T. The $\rho_{cN\infty}/\rho_{cB} \rightarrow 1$ for $N_d > 1 \times 10^{20}$ cm^{-3}, since the current in the NW contact approaches that in the bulk contact, because the NW space-charge distribution at the axis is almost same as in the bulk contact [see Fig. 5(a)] and uniform over most of the NW cross-section except near the surface [see Fig. 5(b)]. However, for higher values of ϕ_{b0}, I_{GR} becomes more and more significant for $N_d \sim 1 \times 10^{18}$ cm^{-3}. Consequently, towards lower doping levels, the $\rho_{cN\infty}/\rho_{cB}$ versus N_d curve for $R = 5$ nm flattens for $\phi_{b0} = 0.6$ V and falls drastically to 0.1 for $\phi_{b0} = 0.8$ V, while the same curve for $R = 10$ nm and $\phi_{b0} = 0.8$ V falls to 0.84.

Figure 10(c) gives the reduction in $\rho_{cN\infty}/\rho_{cB}$ as the surrounding field is reduced by decreasing the contact extension L_E or increasing metal protrusion L_P. The effect of Q_s, shown in Fig. 10(d), can be explained as follows. A Q_s of opposite polarity to that of ionized n-type dopants, i.e., a negative Q_s, depletes the NW which increases the space-charge width at any N_d, reducing I_T and increasing I_{GR} in the NW. At higher N_d where tunneling dominates, reduced I_T raises $\rho_{cN\infty}/\rho_{cB}$; as one moves towards lower N_d, generation-recombination comes into play dropping $\rho_{cN\infty}/\rho_{cB}$. On the other hand, a Q_s of the same polarity as that of ionized n-type dopants reduces the space-charge width, increasing I_T in the NW and hence reducing $\rho_{cN\infty}/\rho_{cB}$. The data given in Figs. 10(c) and 10(d) corresponds to $\phi_{b0} = 0.4$ V, since the data for higher $\phi_{b0} = 0.8$ V was discussed in our prior work.[11]

V. RESULTS AND DISCUSSION FOR A SHORT NANOWIRE

The analysis presented so far pertains to the effects of the surrounding field and surface defects in contacts to long NWs [see Fig. 1(a)] whose length $L_{NW} \gg W_{S\infty}$ is shown in Figs. 6(a) and 6(b). However, in practical contacts with $N_d \leq 10^{19}$ cm^{-3} where $W_{S\infty}$ is high, we may have $L_{NW} \leq W_{S\infty}$. The present section analyzes how reduction of L_{NW} to values comparable to or less than $W_{S\infty}$ [see Fig. 1(b)] affects the space-charge non-uniformity, current non-uniformity, and ρ_{cN}. We anticipate that shortening L_{NW} below $W_{S\infty}$ will reduce the surrounding field effects, making NW contact approach the bulk characteristics. However, as we show, while the resulting change in radial non-uniformity of space-charge is significant, that in similar non-uniformity of the current density is not, and the change in current or ρ_{cN} is disproportionately smaller than that in L_{NW}.

A. Space-charge non-uniformities

Focus on the schematic of the space-charge distribution for short NWs in Fig. 4. The positive distribution corresponds to NW depletion charge associated with the metal contact, and the negative distribution to the inversion charge associated with the NW-substrate junction. The distribution has three critical space-charge widths—W_S, W_A analogous to $W_{S\infty}$, $W_{A\infty}$, respectively, and the distance, W_0, of the zero space-charge point from the metal contact. All these three are $< L_{NW}$, since the edge of this space-charge layer cannot go beyond the edge of the inversion layer formed by the electrons transferred from the heavily doped substrate into the lightly doped NW. We have $W_S > W_A$ for reasons mentioned in Sec. IV for long NWs. However, W_0 at the axis is seen to be the same as that at the surface, the reason for which is clear from the following logic. Suppose, for the metal contact, W_0 at the surface were to exceed that at the axis due to the surrounding field effect, the same condition should hold for W_0 of the NW-substrate junction as well; this is not possible since the sum of the W_0 of the metal contact and that of the NW-substrate junction equals L_{NW}, both at the axis and at the surface.

Figure 11 reports the calculations of the space-charge distribution as L_{NW} is reduced for typical NW contact configurations. The maximum values of L_{NW} in Figs. 11(a) and 11(b) have been chosen as $\approx W_{S\infty}$ of the contact structures in the respective figures. The smaller L_{NW} in Fig. 11(a) have been chosen as $\leq W_{A\infty}$; however, the smaller L_{NW} in Fig. 11(b) is $> W_{A\infty}$ since a NW having $L_{NW} = W_{A\infty} = 16.2$ nm would be too short for practical realization. On reduction in L_{NW}, all the three critical space-charge widths—W_A, W_S, W_0, and the space-charge tails (W_0–W_A) at the axis and (W_0–W_S) at the surface, are seen to fall in Figs. 11(a) and 11(b). However, W_A falls in Fig. 11(a) but not much in Fig. 11(b). This is because the depth of radial penetration of E_r relative to R is more in Fig. 11(a) than in Fig. 11(b) due to the larger L_D/R ratio in the former, where L_D is the Debye length. Figure 12 illustrates that NW shortening reduces the radial non-uniformity of the space-charge width defined by the ratio W_S/W_A, due to the reduction in surrounding field effects, and shifts the N_d at which the peak non-uniformity is attained to higher doping levels. The reduction in non-uniformity can be understood with the help of Fig. 1(b), where some of the field lines terminating on the metal

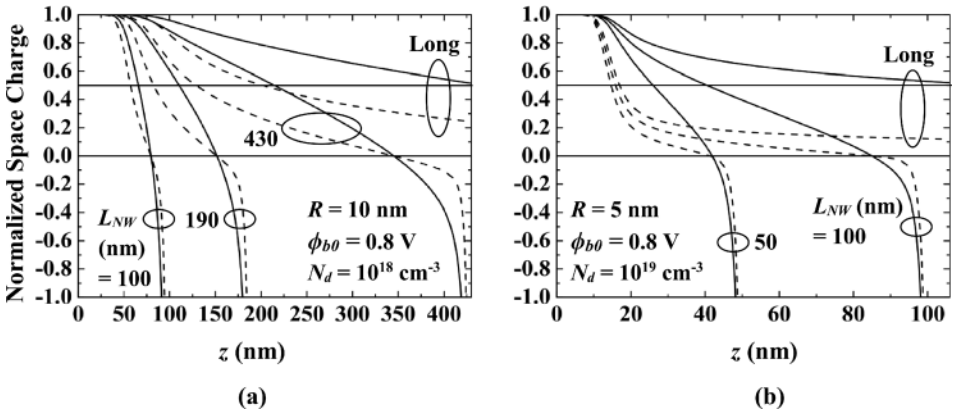

FIG. 11. Simulated normalized space-charge distribution along the axis (dashed line) and surface (solid line) as a function of distance from the contact, for different NW lengths, L_{NW}. Space-charge edge is located at the point of intersection of the distribution with the horizontal line at normalized space charge = 0.5. See the first para of Sec. IV for values of parameters other than those shown here.

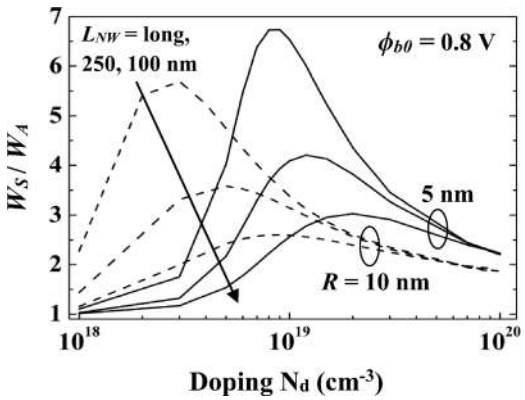

FIG. 12. Simulated reduction in radial non-uniformity of the space-charge width as the NW length is reduced. The non-uniformity is represented by the ratio of the space-charge width at the surface, W_S, to that at the axis, W_A. See the first para of Sec. IV for values of parameters other than those shown here.

contact come from the n^+ substrate rather than the NW, reducing the surrounding field effects on the NW.

B. Current non-uniformities

Figure 8 showed the axial distribution of the I_{GR} dominated current density, $|J_z|$, in a long NW, directed along the NW length at the axis and the surface. The changes in this distribution due to NW shortening are shown in Fig. 13(a). The current density falls because a reduction in space-charge width lowers the GR current. The location near the contact, where the $|J_z|$ distribution at the axis crosses that at the surface, moves closer to the contact. A similar cross-over point appears near the NW-substrate junction where the radial electric field is inwards, i.e., in a direction opposite to that near the contact [see Fig. 1(b)]. The electrons generated near the contact move towards the NW-substrate junction; on entering the junction space-charge region, they are moved towards the surface by the inward radial field, increasing the current density at the surface.

Figure 13(b) shows the detailed radial variation of $|J_z|$ in a normalized form for the NW contact configurations considered in Fig. 11. As L_{NW} is reduced, W_A and W_S fall, raising the tunneling current but reducing the GR current. Hence, if a contact is tunneling dominated in the long NW case, it would continue to be so on shortening of the NW; for this reason, the contact of Fig. 11(b) is tunneling dominated for all L_{NW}. As far as the contact of Fig. 11(a) is concerned, it is GR dominated in the long NW case; since GR current reduces on shortening the NW, we used simulation to confirm that it is indeed GR dominated for all L_{NW} considered in this figure. It is interesting to note that, while the radial distribution of *absolute* $|J_z|$ and hence contact resistivity ρ_{cN} are affected by reduction in L_{NW}, the radial distribution of *normalized* $|J_z|$, shown in Fig. 13(b), which reflects the radial current non-uniformity is seen to be relatively insensitive to L_{NW} in both tunneling and GR dominated contacts. The reason for this is that, as argued in Sec. IV C, the current non-uniformity arises from G_T *non-uniformity* and radial electric field *close to the metal contact*, where they are not affected much by reduction in L_{NW}. In contrast, the radial non-uniformity in the space-charge width discussed above is significant since it arises from the radial electric field *away from the contact*, which depends on L_{NW}.

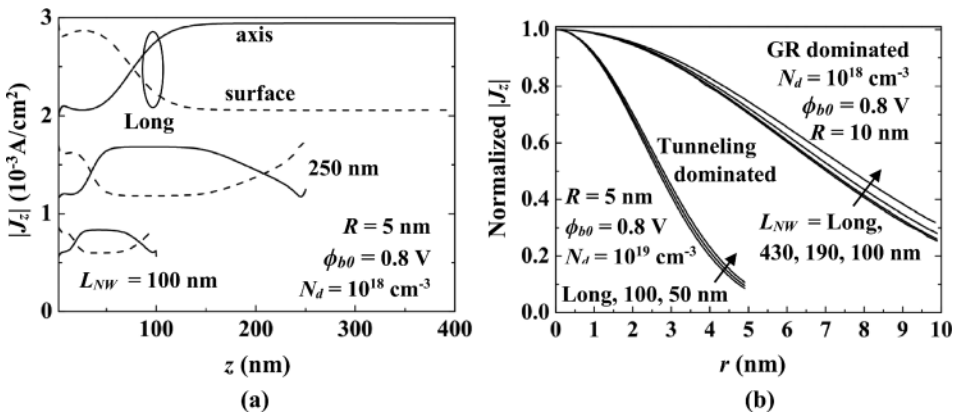

FIG. 13. (a) Comparison of axial current density along the NW axis and surface in contacts to NWs of different lengths L_{NW}, where generation-recombination dominates over tunnelling. (b) Radial non-uniformity of the axial current density at different L_{NW} for contacts with tunnelling and GR dominated current. See the first para of Sec. IV for values of parameters other than those shown here.

C. Contact resistivity

Simulations show that the resistivity of the NW-substrate junction is much less than the ρ_{cN} of the metal contact being studied. The simulated changes in ρ_{cN} due to shortening of L_{NW} are reported in Fig. 14 for a variety of NW contact structures. The values of N_d, ϕ_{b0}, R, and L_{NW} chosen are such that L_{NW} is realizable and comparable to or less than $W_{S\infty}$, and both GR dominated and tunneling dominated contacts are covered. It is seen that, in the range of L_{NW} considered, the changes in L_{NW} do not alter the dominant current mechanism. Further, the reduction in L_{NW} increases the ρ_{cN} of GR dominated contacts (curves *a*, *b*), and reduces the ρ_{cN} of tunneling dominated contacts (curves *c*, *d*); this can be attributed to the fall in GR current but rise in tunneling current on reduction in space-charge width. On the other hand, consider fixing L_{NW} and altering N_d, ϕ_{b0} or R so as to increase $W_{S\infty}$ or $W_{A\infty}$. Such changes are seen to reduce ρ_{cN} if the contact remains tunneling dominated in spite of the changes (curves *c*, *d*), but increase ρ_{cN} if either the contact remains GR dominated (curves *a*, *b*) or changes from tunneling dominated to GR dominated (pairs of curves *a*, *c* or *a*, *d* or *b*, *c* or *b*, *d*).

Consider the contacts showing maximum changes in ρ_{cN} with NW shortening (curves *a* and *d*). We find that, the 6 times change in the ρ_{cN} of GR dominated contact is $\ll$20 times change in L_{NW} from 1013 nm ($=W_{S\infty}$) to 50 nm, and the 1/0.43 = 2.3 times change in the ρ_{cN} of tunneling dominated contact is $\ll$9.7 times change in L_{NW} from 486 nm ($=W_{S\infty}$) to 50 nm. The reason why the change in current or ρ_{cN} is disproportionately smaller than that in L_{NW} is that both GR and tunneling occur over a small fraction of the space-charge width near the junction (see Sec. IV B) that is not affected much by NW length reduction.

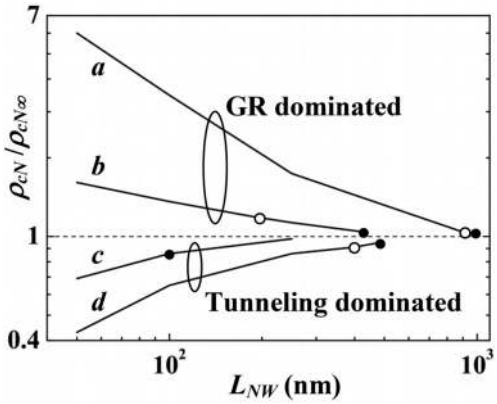

Curve	*a*	*b*	*c*	*d*
N_d (cm^{-3})	10^{18}	10^{18}	10^{19}	10^{18}
ϕ_{b0} (V)	0.8	0.8	0.8	0.4
R (nm)	5	10	5	5

FIG. 14. Change in contact resistivity, ρ_{cN}, due to shortening of the NW length, L_{NW}; contact resistivity for the long NW case is denoted as $\rho_{cN\infty}$; the solid circle represents the data for $L = W_{S\infty}$ and open circle that for $L = W_{A\infty}$; the NW ambient is SiO_2 and $T = 300$ K. See Figs. 6(a) and 6(b) for values of $W_{S\infty}$ and $W_{A\infty}$, and the first para of Sec. IV for values of NW parameters other than those shown here.

VI. SUMMARY AND CONCLUSION

We simulated numerically the effects of the surrounding field and surface defects on small-bias space-charge and current distributions of *end-bonded* metal contacts having a wide range of intrinsic barrier heights $\phi_{b0} = 0.4$–0.8 V on *thin* n-type silicon NanoWires (NWs) of radius $R = 5$–10 nm and *heavy* doping of $N_d = 10^{18}$–10^{20} cm^{-3}, embedded in SiO_2. We found the following qualitative and quantitative trends at room temperature.

The surrounding field causes significant *radial* non-uniformities in space-charge and current distributions for doping $N_d > 10^{18}$ cm^{-3}. This is intriguing since theoretical nanowire analyses in literature, by and large restricted to $N_d < 10^{18}$ cm^{-3}, have found these distributions to be approximately uniform, used this condition to develop an analytical model of the NW junction, and focused their attention on the enhancement of the space-charge and its *axial* rather than radial non-uniformity. When the NW is long, the metal size is large and charge on the nanowire surface is negligible, the space-charge non-uniformity peaks at N_d for which the bulk depletion width $\approx 2.14R$. At this peak point, for $\phi_{b0} = 0.4$ (0.8) V, the space-charge width at the surface is $\sim$3 times (6–7 times) that at the axis, while the current density at the axis is $\sim$2.5 times (10–13 times) that at the surface.

The energy location of tunneling is near the top, middle, and bottom of the barrier for $N_d = 10^{18,19,20}$ cm^{-3}, while the physical location of generation-recombination is near the junction within 12% of the space-charge width. For $\phi_{b0} = 0.8$ V and N_d up to 3–5 $\times 10^{18}$ cm^{-3}, both tunneling and generation-recombination influence the NW contact resistivity, $\rho_{cN\infty}$, causing it to vary slowly or even increase, so that for $R = 5$ (10) nm, $\rho_{cN\infty}$ is 10 (1.2) times lower at $N_d = 10^{18}$ cm^{-3} but 195 (12) times higher than the bulk contact resistivity, ρ_{cB}, at $N_d = 10^{19}$ (4×10^{18}) cm^{-3}. However, generation-recombination falls rapidly as ϕ_{b0} is reduced or N_d is raised. Hence, for $\phi_{b0} = 0.8$ V and $N_d > 5 \times 10^{18}$ cm^{-3} or $\phi_{b0} \leq 0.6$ V and all N_d, independent of R, $\rho_{cN\infty}$ is governed by tunneling alone, and so, falls rapidly and monotonically with N_d. For $R = 5$ nm and $N_d = 10^{18}$ (10^{19}) cm^{-3}, $\rho_{cN\infty}/\rho_{cB} = 44$ (32) at $\phi_{b0} = 0.6$ V and 18 (7) at $\phi_{b0} = 0.4$ V. The $\rho_{cN\infty}/\rho_{cB}$ falls to 1.5–2.5 at $N_d = 10^{20}$ cm^{-3} for all ϕ_{b0} and R.

Practical contacts with $N_d \leq 10^{19}$ cm^{-3} may have a NW length $L_{NW} \leq$ long NW space-charge width. In such contacts, shortening the L_{NW} reduces the surrounding field effects, making NW contact approach the bulk characteristics. Thus, the radial non-uniformity in space-charge is reduced, the current in GR dominated contacts falls increasing their ρ_{cN}, while the current in tunneling dominated contacts rises decreasing their ρ_{cN}. On the other hand, if L_{NW} is fixed and N_d, ϕ_{b0} or R are altered so as to increase the long NW space-charge width, ρ_{cN} reduces if the contact remains tunneling dominated in spite of the changes, but increases if either the contact remains GR dominated or changes from tunneling dominated to GR dominated. However, while the current is

affected, its radial non-uniformity is not, and the change in current or ρ_{cN} is disproportionately smaller than that in L_{NW}; e.g., for $R = 5$ nm, $\phi_{b0} = 0.8$ V and $N_d = 1 \times 10^{18}$ cm^{-3}, 20 times reduction in L_{NW} (from 1 μm to 50 nm) causes 6 times increase in ρ_{cN}. This is because the region over which tunneling or GR causing the current and its non-uniformity occur is small and located near the junction; this region is therefore less affected by NW shortening.

Our insights and data regarding the space-charge, current, and contact resistance variations for different N_d, ϕ_{b0}, R, and L_{NW} are useful in different ways. They provide an experimentalist clear qualitative understanding over a wide range of conditions. They are also helpful in the design, characterization, and analytical modeling of NW devices. Our calculations take into account the effects of the surrounding field, surface charge and recombination, contact geometry, dielectric confinement, image force barrier lowering, and heavy doping.

ACKNOWLEDGMENTS

The authors would like to thank Dr. Vijaya Kumar Gurugubelli for useful discussions in the domain of nanowire junctions.

APPENDIX: SIMULATION METHODOLOGY

We have used TCAD SENTAURUS[31] for our simulations. This simulator simultaneously solves the Poisson's equation, the drift-diffusion current density equations, and continuity equations for electrons and holes numerically, both inside and outside the NW for an applied reverse bias of thermal voltage indicative of a small bias. Inclusion of the outside dielectric in the simulation is crucial for taking the surrounding field into account. We take into account the heavy doping effects of partial impurity ionization, impurity band formation, Fermi-Dirac statistics, and bandgap narrowing (as per Slotboom's model[31]). While estimating impurity ionization, increase in ionization energy due to dielectric confinement[15,28,29] is taken into account. As is known,[15,22] quantum confinement effects can be ignored in Si NWs with $R \geq 5$ nm.

With regards to the boundary conditions, at the metal-semiconductor junction, the potential is taken as the sum of the built-in potential and applied reverse bias, implying thereby that the potential is zero far away from the junction. The electron and hole densities at this junction are decided by the thermionic emission-diffusion theory[12] with image force barrier lowering, $\Delta\phi = \sqrt{qE/4\pi\varepsilon_s}$, where E is the junction field. The electron and hole current density normal to the NW surface are zero. Across this surface, the tangential electric field is assumed to be continuous and the normal displacement vector is assumed to be discontinuous by an amount equal to Q_s.

The equations for the tunneling equivalent generation rate G_T, SRH generation rate G_{SRH}, ionization energy E_{ion} including dielectric confinement, and the thermionic emission-diffusion boundary condition have been detailed in Sec. IV of our previous work.[11] The following parameter values are used in these equations. The G_T is calculated using a doping and temperature independent tunneling effective mass $m = 0.3m_0$ for silicon.[14,33] The G_{SRH} is determined assuming the recombination center at the intrinsic level, $\tau_n = \tau_p = \tau_B = 1$ μs for bulk junctions, and $s = 2.5 \times 10^5$ cm/s based on the value extracted from measurements in Ref. 6 (this gives $\tau_N = 1$, 2 ps for $R = 5$, 10 nm). The effective Richardson constant for electron tunneling in silicon[12] was assumed as $A^* = 270$ A cm^{-2} K^{-2} at $T = 300$ K. The dielectric confinement formula[15,28,29] predicts an increase in E_{ion} of phosphorus in silicon at low N_d from 45 meV in bulk to 85 meV in a NW with $R = 5$ nm and surrounded by SiO_2 ambient; analogous numbers for $N_d = 10^{18}$, 10^{19}, and 10^{20} cm^{-3} are $E_{ion} = 55$, 18, and -59 meV.

[1]S. Sett, K. Das, and A. K. Raychaudhuri, J. Appl. Phys. **121**, 124503 (2017).
[2]S. E. Mohney, Y. Wang, M. A. Cabassi, K. K. Lew, S. Dey, J. M. Redwing, and T. S. Mayer, Solid-State Electron. **49**, 227 (2005).
[3]A. Chaudhry, V. Ramamurthi, E. Fong, and M. Saif Islam, Nano Lett. **7**, 1536 (2007).
[4]F. Léonard and A. A. Talin, Nat. Nanotechnol. **6**, 773 (2011).
[5]C. Fernandes, A. Shik, K. Byrne, D. Lynall, M. Blumin, I. Savaliev, and H. E. Ruda, Nanotechnology **26**, 085204 (2015).
[6]F. Léonard, A. A. Talin, B. Swartzentruber, and S. Picraux, Phys. Rev. Lett. **102**, 106805 (2009).
[7]J. Hu, Y. Liu, C. Z. Ning, R. Dutton, and S. M. Kang, Appl. Phys. Lett. **92**, 083503 (2008).
[8]E. Stern, G. Cheng, M. P. Young, and M. A. Reed, Appl. Phys. Lett. **88**, 053106 (2006).
[9]X. L. Han, G. Larrier, E. Dubois, and F. Cristiano, Surf. Sci. **606**, 836 (2012).
[10]D. Erts, B. polyakov, B. Daly, M. A. Morris, S. Ellingboe, J. Boland, and J. D. Holmes, J. Phys. Chem. B **110**, 820 (2006).
[11]A. A. Shukkoor and S. Karmalkar, J. Appl. Phys. **122**, 214501 (2017).
[12]S. M. Sze and K. K. Ng, *Physics of Semiconductor Devices* (Wiley India, New Delhi, 2007).
[13]A. Y. C. Yu, Solid-State Electron. **13**, 239 (1970).
[14]C. Y. Chang, Y. K. Fang, and S. M. Sze, Solid-State Electron. **14**, 541 (1971).
[15]V. Schmidt, J. V. Wittemann, S. Senz, and U. Gösele, Adv. Mater. **21**, 2681 (2009).
[16]L. Li, Y. Fang, C. Xu, Y. Zhao, N. Zang, P. Jiang, and K. J. Ziegler, Nanotechnology **27**, 165303 (2016).
[17]S. A. Dayeh, R. Chen, Y. G. Ro, and J. Sim, Mater. Sci. Semicond. Process. **62**, 135 (2017).
[18]H. Schmid, M. T. Bjork, J. Knoch, S. Karg, H. Riel, and W. Riess, Nano Lett. **9**, 173 (2009).
[19]M. Berg, J. Svensson, E. Lind, and L.-E. Wernersson, Appl. Phys. Lett. **107**, 232102 (2015).
[20]S. Zhu, J. Chen, M. F. Li, S. J. Lee, J. Singh, C. X. Zhu, A. Du, C. H. Tung, A. Chin, and D. L. Kwong, IEEE Electron Device Lett. **25**, 565 (2004).
[21]M. Jang, Y. Kim, J. Shin, and S. Lee, IEEE Electron Device Lett. **26**, 354 (2005).
[22]V. K. Gurugubelli and S. Karmalkar, J. Appl. Phys. **119**, 024507 (2016).
[23]V. Schmidt, S. Senz, and U. Gösele, Appl. Phys. A **86**, 187 (2007).
[24]I. Kimukin, M. S. Islam, and R. S. Williams, Nanotechnology **17**, S240 (2006).
[25]K. Seo, S. Sharma, A. A. Yasseri, D. R. Stewart, and T. I. Kamins, Electrochem. Solid State Lett. **9**, G69 (2006).
[26]V. K. Gurugubelli and S. Karmalkar, Appl. Phys. Lett. **104**, 203502 (2014).
[27]P. Agarwal, M. Vijayaraghavan, F. Neuilly, E. Hijzen, and G. Hurkx, Nano Lett. **7**, 896 (2007).
[28]Y. M. Niquet, A. Lherbier, N. H. Quang, M. V. Fernandes-Serre, X. Blase, and C. Delerue, Phys. Rev. B **73**, 165319 (2006).
[29]M. Diarra, Y. M. Niquet, C. Delerue, and G. Allan, Phys. Rev. B **75**, 045301 (2007).
[30]E. C. Garnett and P. Yang, J. Am. Chem. Soc. **130**, 9224 (2008).
[31]Synopsys, *Sentaurus Device User Guide* (Synopsys, 2015).
[32]N. Stavitski, M. J. H. van Dal, A. Lauwers, C. Vrancken, A. Y. Kovalgin, and R. A. M. Wolters, IEEE Electron Device Lett. **29**, 378 (2008).
[33]K. K. Ng and R. Liu, IEEE Trans. Electron Devices **37**, 1535 (1990).

[34]Q. Gao, Y. Ouyang, and G. Jing, J. Appl. Phys. **109**, 104307 (2011).
[35]P. U. Calzolari and S. Graffi, Solid-State Electron. **15**, 1003 (1972).
[36]S. Petrosyan and A. Y. Shik, Sov. Phys. JETP **69**, 1261 (1989) [Zh. Eksp. Teor. Fiz. **96**, 2229–2239 (1989)].
[37]H. Ruda and A. Shik, J. Appl. Phys. **84**, 5867 (1998).
[38]M. Ieong, P. M. Solomon, S. E. Laux, H.-S. P. Wong, and D. Chidambarrao, in International Electron Devices Meeting, Technical Digest (1998), p. 733.
[39]H. Park, R. Beresford, S. Hong, and J. Xu, J. Appl. Phys. **108**, 094308 (2010).